Estimating the Green's function using a single channel dual-beam interferometer

Sam Hitchman,[1,a)] Kasper van Wijk,[1] and Roel Snieder[2]
[1]*Faculty of Science, Department of Physics, Dodd-Walls Centre for Photonic and Quantum Technologies, University of Auckland, Private Bag 92019, Auckland 1010, New Zealand*
[2]*Center for Wave Phenomena, Colorado School of Mines, Golden, Colorado 80401-1887, USA*

(Received 15 February 2018; revised 5 June 2018; accepted 17 June 2018; published online 6 July 2018)

Cross-correlation of independent, equipartitioned wavefields is a well-established method to estimate the elastic Green's function, commonly termed seismic interferometry. In this article, the sum of a wavefield recorded at two locations in a single channel is used to estimate the Green's function via the autocorrelation; the result contains some predicted artefacts. The underlying theory and hardware required to estimate the Green's function is presented and compared to traditional seismic interferometry. This technique is used to estimate the elastic Green's function between two locations on an aluminum block with surface scatterers. Wavefields excited via rapid thermoelastic expansion of the surface using a pulsed laser are detected by a dual-beam heterodyne interferometer. The detector is capable of directly recording the sum of a wavefield measured at two locations in a single channel. This method could be an effective, low cost, and non-contacting technique for structural monitoring, particularly where ambient noise has established equipartitioned wavefields in the structure. © *2018 Acoustical Society of America*. https://doi.org/10.1121/1.5045329

[KGS] Pages: 124–130

I. INTRODUCTION

Over the past decade, Green's function retrieval by cross-correlation of wavefields recorded at independent receivers has become an important tool in seismic monitoring and non-destructive testing.[1–3] The wavefields could consist of ambient noise[4–6] or be generated from transient sources.[7,8] For Green's function retrieval from ambient noise, time synchronized signals from each receiver are cross-correlated to extract the Green's function.[4,9] For transient sources, the Green's function can be estimated by summing the cross-correlation of the response recorded between receivers if the sources are located on a contour [in two dimensions (2D)] or a surface [in three dimensions (3D)] that surrounds the receivers.[8,10] The direct arrival of the Green's function can be used to estimate the bulk elastic properties of the sample, and the coda consists of scattered waves. Differences in the Green's function under the influence of external factors (time, stress, or temperature) can therefore be used for time-lapse monitoring.[11–13] Here, we estimate the Green's function between two receivers that are simultaneously recorded on a single channel. In the case of a single channel recording of two wavefields, we show that the autocorrelation of the recording is proportional to the Green's function between receivers, with some additional artefacts.

We amend the underlying theory for seismic interferometry for independent receivers for the new case of two receivers recorded in a single channel. Next, we show the design and discuss the inner workings of a non-contacting laser Doppler vibrometer modified to simultaneously record the surface velocity of two locations on a sample surface. To validate the theory and hardware we extract the Rayleigh wave Green's function between two locations on an aluminum block with surface scatterers. Elastic waves are generated via thermo-elastic expansion of the aluminum surface due to the absorption of a high energy pulse of light.

This hardware and analysis could be used for non-contact structural monitoring. In the case of monitoring of a concrete bridge, for example, it has been shown that traffic-induced vibrations detected at multiple contacting accelerometers can be cross-correlated to estimate the Green's function.[14] Over time, stress induced cracking of concrete causes a decrease in the elastic wave speeds and an increase in attenuation, both of which can be monitored by comparing the Green's function direct arrival and coda as a function of time.[15] Seismologists have used ambient noise and earthquake coda, which consist of many scattered events, to successfully monitor changes in the subsurface of the Earth. An excellent example of subsurface monitoring over time is presented by Sens-Schönfelder and Wegler,[6] who compare the estimated Green's function for each day to a reference recording to monitor changes in the subsurface near Merapi Volcano, Indonesia. Variations in the Green's function estimated by passive seismic interferometry strongly agreed with results found in an independent active coda-wave interferometry experiment.[16]

II. THEORY OF SEISMIC INTERFEROMETRY

Weaver and Lobkis[17] showed that for a finite body the cross-correlation of an equipartitioned wavefield at two receivers provides the Green's function. Because equipartitioned wavefields are difficult to produce in a laboratory setting, we consider the case of many transient sources located on a contour that surrounds a pair of receivers. For a

[a)]Electronic mail: sam.hitchman@auckland.ac.nz

 0001-4966/2018/144(1)/124/7/$30.00

transient source located at $\boldsymbol{x}$ the observed wavefield recorded by a receiver located at $\boldsymbol{x}_A$ is given by

$$U(\boldsymbol{x}_A, \boldsymbol{x}, \omega) = G(\boldsymbol{x}_A, \boldsymbol{x}, \omega) s(\omega), \tag{1}$$

where $G(\boldsymbol{x}_A, \boldsymbol{x}, \omega)$ is the impulse response and $s(\omega)$ is the Fourier transform of the source-time function. According to Eq. (80) of Wapenaar and Fokkema,[10] the velocity Green's function between two receivers, $G(\boldsymbol{x}_A, \boldsymbol{x}_B, \omega)$, can be approximated by the cross-correlation of the velocity wavefields $U(\boldsymbol{x}_A, \boldsymbol{x}, \omega)$ and $U(\boldsymbol{x}_B, \boldsymbol{x}, \omega)$, which are surrounded by uncorrelated sources on a surface δD,

$$2\Re\big[G(\boldsymbol{x}_A, \boldsymbol{x}_B, \omega)\big] S(\omega) \approx \frac{2}{\rho c} \oint_{\delta D} U^*(\boldsymbol{x}_A, \boldsymbol{x}, \omega) U(\boldsymbol{x}_B, \boldsymbol{x}, \omega) \delta^2 \boldsymbol{x}, \tag{2}$$

where $\Re$ represents the real part, U^* is the complex conjugate of U and $S(\omega) = s^*(\omega) s(\omega)$ is the power spectrum of the source wavelet. ρ and c represent the density and elastic wave speed of the medium, respectively. In practice Eq. (2) implies that in the time-domain Green's function retrieval from transient sources requires many excitation locations and two independently recorded receivers. In situations where there are constraints on time and/or a limited number of receivers/sources are available, Green's function retrieval may be inaccurate. We propose to record the sum of $U(\boldsymbol{x}_A, \boldsymbol{x}, \omega)$ and $U(\boldsymbol{x}_B, \boldsymbol{x}, \omega)$ in a single channel to estimate $G(\boldsymbol{x}_A, \boldsymbol{x}_B, \omega)$. Recording the sum of a wavefield measured at two locations halves the data size and hardware required for Green's function retrieval. The single channel, two location recorded wavefield $U_{AB}(\omega)$ is defined by

$$U_{AB}(\boldsymbol{x}, \omega) = U(\boldsymbol{x}_A, \boldsymbol{x}, \omega) + U(\boldsymbol{x}_B, \boldsymbol{x}, \omega). \tag{3}$$

Because the sum of the waves at both receivers is recorded on a single channel for each source location, we use the autocorrelation function instead of the cross-correlation. The autocorrelation of $U_{AB}(\omega)$ when integrated over source locations can, with Eq. (2), be written as

$$\begin{aligned} &4\Re\big[G(\boldsymbol{x}_A, \boldsymbol{x}_B, \omega)\big] S(\omega) + 2\Re\big[G(\boldsymbol{x}_A, \boldsymbol{x}_A, \omega)\big] S(\omega) \\ &\quad + 2\Re\big[G(\boldsymbol{x}_B, \boldsymbol{x}_B, \omega)\big] S(\omega) \\ &\approx \frac{2}{\rho c} \oint_{\delta D} U^*_{AB}(\boldsymbol{x}, \omega) U_{AB}(\boldsymbol{x}, \omega) \delta^2 \boldsymbol{x}, \end{aligned} \tag{4}$$

where $G(\boldsymbol{x}_A, \boldsymbol{x}_A, \omega) S(\omega)$ and $G(\boldsymbol{x}_B, \boldsymbol{x}_B, \omega) S(\omega)$ are the response of coinciding source/receiver, with power density spectra $S(\omega)$, located at $\boldsymbol{x}_A$ and $\boldsymbol{x}_B$, respectively.

III. A DUAL-BEAM VIBROMETER

We present a dual-beam laser Doppler vibrometer (DB-LDV) designed to simultaneously record the particle velocity at two locations on a single channel. To validate the DB-LDV and the use of the autocorrelation to approximate $G(\boldsymbol{x}_A, \boldsymbol{x}_B, \omega)$, we excite elastic waves in an aluminum block with surface scatterers. This experiment is reciprocal to that presented by Mikesell *et al.*[8] They showed that the autocorrelation of recorded wavefields can be used to locate scatterers in a heterogeneous sample, and the cross-correlation of wavefields at two source locations is an accurate estimate of the direct and scattered waves. First, we describe the operation of traditional laser Doppler vibrometers (LDVs) and the modifications required to record two channels simultaneously. LDVs are optical devices that measure the surface particle velocity of a sample using a reflected laser beam.[18,19] LDVs have been used to characterize the elastic response of fruit,[20,21] rocks,[22] structures,[23,24] and soft tissue phantoms.[25] Typically, LDVs generate a beam of light that has a modulated intensity pattern, $I(t)$. The frequency of the oscillation contains information about the surface vibration of the sample. The design and operation of a home-built single-beam LDV has been presented by Hitchman *et al.*[18] The LDV splits light into a reference beam, which has a known path length and frequency, and a sample beam, which is reflected by the sample. When the sample surface is in motion, the sample beam frequency is Doppler shifted. In the time domain the Doppler shift of the sample beam, f_{Dx_A} is related to the surface particle velocity $u(\boldsymbol{x}_A, \boldsymbol{x}, t)$ by

$$f_{Dx_A} = \frac{2u(\boldsymbol{x}_A, \boldsymbol{x}, t)}{\lambda} \cos(\theta - \pi), \tag{5}$$

where λ is the wavelength of the laser used and θ is the angle between the direction of the surface motion and the laser beam. Equation (5) shows that when the surface of the sample moves away from the laser, that is $\theta = \pi = 180^\circ$, the sample beam is red-shifted and decreases in frequency. When the sample moves toward the laser beam blue-shift occurs. In this article, we only consider normal incidence to the sample surface. For lasers that operate in the visible spectrum, the frequency of the emitted photons is on the order of 10^{15} Hz. Changes to the nominal frequency due to sample motion therefore cannot be detected using current electronic devices. To measure f_{Dx_A} and extract $u(\boldsymbol{x}_A, \boldsymbol{x}, t)$ the sample beam is added to a frequency-shifted reference beam resulting in a detected intensity pattern, $I(t)$, which beats at a frequency equal to the magnitude of difference between the photon frequency of the reference beam and the sample beam

$$\begin{aligned} I(t) &= A \cos\left[2\pi \left| \left(\frac{c}{\lambda} + f_{\text{ref}}\right) - \left(\frac{c}{\lambda} + f_{Dx_A}(t)\right) \right| t\right] \\ &= A \cos\big[2\pi \big(|f_{\text{ref}} - f_{Dx_A}(t)|\big) t\big], \end{aligned} \tag{6}$$

where f_{ref} is the frequency deviation of the reference beam and A is the amplitude of the intensity pattern, determined primarily by the amount of light reflected by the sample. The reference beam is frequency shifted using an acousto-optic modulator (AOM) in order to avoid directional ambiguity of the sample motion due to the absolute value in Eq. (6).[18] The c/λ term is the nominal frequency of the laser, where c is the speed of light and λ is the laser wavelength. The c/λ terms cancel when interfering with the reference and sample beams, as shown in Eq. (6). We modify the LDV presented by Hitchman *et al.*[18] to form a DB-LDV capable of detecting the sum of the surface vibrations at two locations. Figure 1 shows

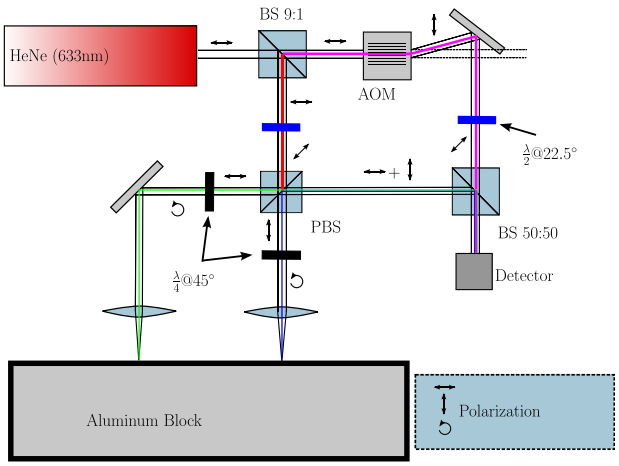

FIG. 1. (Color online) A schematic of the dual-beam interferometer used for single channel acquisition of a wavefield measured at two locations. The sample arm (red) is split using a polarizing beam splitter (PBS), causing the light for the two subsequent sample beams (green and blue) to be orthogonally polarized. Light reflected from the sample is Doppler shifted due to the surface motion of the sample. The sample beams are recombined at the PBS but do not interfere with each other due to the polarization of each beam. A reference beam (purple) is also shifted using an AOM and the polarization is set to 45° relative to each sample arm. The reference beam and sample beams are combined using a 50:50 beam splitter (BS). The resulting interference pattern, $I(t)$, is an oscillation where the instantaneous frequency is equal to the mean of the Doppler shifted sample beams and plus the reference arm frequency shift.

the design of the dual-beam interferometer. The sample beam is split into two orthogonally polarized beams using a polarizing beam splitter (PBS) and focused on to the sample surface. Light, which is backscattered off the surface at two different locations, is collected by the focusing lenses and the beams are recombined at the PBS. These beams do not interfere with one another due to their orthogonal polarizations. Separating beams by polarization rather than spatial positioning is often termed polarization-division multiplexing, a technique commonly used in fiber-optic communication where light is confined to the optical fiber core.[26] The recombined beams are mixed with the reference beam set to 45° relative to both sample beams using a 50:50 beam splitter (BS). The interference pattern, $I_{\text{dual}}(t)$, at the detector is given by

$$I_{\text{dual}}(t) = A\cos\left[2\pi(|f_{\text{ref}} - f_{Dx_A}(t)|)t\right] + B\cos\left[2\pi(|f_{\text{ref}} - f_{Dx_B}(t)|)t\right], \quad (7)$$

where f_{ref} is the frequency shift of the reference beam and $f_{Dx_A}(t)$ and $f_{Dx_B}(t)$ are the Doppler shifts due to wavefields $u(\boldsymbol{x}_A, \boldsymbol{x}, t)$ and $u(\boldsymbol{x}_B, \boldsymbol{x}, t)$, respectively. Setting amplitudes A and B to 1 results in an interference pattern given by

$$I_{\text{dual}}(t) = 2\cos\left[2\pi\left(f_{\text{ref}} - \frac{|f_{Dx_A}(t) + f_{Dx_B}(t)|}{2}\right)t\right] + \cos\left[2\pi\left(\frac{|f_{Dx_A}(t) - f_{Dx_B}(t)|}{2}\right)t\right]. \quad (8)$$

Equation (8) shows that the interference pattern of the dual-beam laser Doppler vibrometer is a frequency modulated (FM) signal, similar to an FM radio signal. Here, the instantaneous frequency of $I_{\text{dual}}(t)$ is $f_{\text{ref}} - |f_{Dx_A}(t) + f_{Dx_B}(t)|/2$. There is also a time-variant envelope of $\cos[2\pi(|f_{Dx_A}(t) - f_{Dx_B}(t)|)t/2]$. The instantaneous frequency of $I_{\text{dual}}(t)$, which contains information about surface motion, can be extracted using IQ demodulation.[27] IQ demodulation extracts the instantaneous frequency using the detected FM signal, typically termed I, and a 90° phase shifted version of I termed Q. The instantaneous frequency of $I_{\text{dual}}(t)$ can be calculated using the following expression:

$$f_{\text{ref}} - \frac{|f_{Dx_A}(t) + f_{Dx_B}(t)|}{2} = \frac{I_{\text{dual}}(t)\dfrac{dQ}{dt} + Q(t)\dfrac{dI_{\text{dual}}}{dt}}{I_{\text{dual}}(t)^2 + Q(t)^2}. \quad (9)$$

Equation (5) can be rearranged to relate $u(\boldsymbol{x}_A, \boldsymbol{x}, t) + u(\boldsymbol{x}_B, \boldsymbol{x}, t)$ to the frequency of $I_{\text{dual}}(t)$,

$$u(\boldsymbol{x}_A, \boldsymbol{x}, t) + u(\boldsymbol{x}_B, \boldsymbol{x}, t) = 2\left[f_{Dx_A}(t) + f_{D_B}(t)\right]\lambda - f_{\text{ref}}, \quad (10)$$

where λ is the wavelength of the laser used and f_{ref} is given by the driven frequency of the AOM (Fig. 1). In practice, the signal is recorded and digitized by a computer and a peripheral component interconnect express (PCIE) based data acquisition card (PCIE-DAQ), where the discrete form of Eq. (9) can be implemented. Note that the signal-to-noise ratio (SNR) of $I_{\text{dual}}(t)$ is increased by a factor of 4 relative to the single-beam interference pattern $I(t)$ in Eq. (6). This is due to (1) splitting of the sample beam and (2) reduced interference due to reference beam polarization. The setup of the dual-beam interferometer is drawn in Fig. 1. The sample arm (red) is split into two subsequent sample beams (green, blue), which are focused on to the surface of a sample. The spacing between sample beams at the surface of the aluminum block can be varied using an adjustable mirror. Backscattered light from the sample is Doppler shifted if the surface is vibrating, encoding the surface motion into the oscillation frequency of the sample beams. Because the sample beams are orthogonally polarized they do not interfere with each other, simplifying the final intensity pattern. A reference beam (purple) is frequency shifted using an AOM and the polarization is set to 45° relative to both sample arms. Both sample beams and the reference beam are combined using a BS. The resulting interference pattern, $I_{\text{dual}}(t)$, is an oscillation where the instantaneous frequency is equal to the combination of the Doppler shifts: $f_{\text{ref}} - |f_{Dx_A}(t) + f_{Dx_B}(t)|/2$. The legend shows the polarization orientation of each beam at different stages of the interferometer. The circular arrow depicts circular polarization, and the straight arrows depict linearly polarized light at different orientation angles. The polarization is controlled using $\lambda/4$ and $\lambda/2$ waveplates.

IV. APPLICATION: SURFACE WAVE SCATTERING IN AN ALUMINUM BLOCK

An aluminum block (280 mm × 230 mm × 215 mm) with cylindrical holes of 1 mm diameter and 3 cm in depth has previously been used to estimate the Rayleigh wave Green's function between two surface locations.[8] In the

same block, we excite elastic waves with a pulsed Nd:YAG 1064-nm laser focused to a 1 mm beam diameter on the block surface (Fig. 2). Localized heating of the block due to laser-light absorption causes thermoelastic expansion and generates broadband ultrasonic waves.[19] A scanning mirror system is used to move the source location in a circle surrounding the holes. The dual-beam interferometer described in Sec. III records ultrasonic waves at locations $\boldsymbol{x}_A$ and $\boldsymbol{x}_B$. A depiction of the setup is presented in Fig. 2. Our experiment is similar and reciprocal to that presented by Mikesell *et al.*,[8] where the receiver was translated in a series of line scans to encompass a fixed source. Automation of our translation and data acquisition is controlled with PLACE, a python-based laboratory automation toolkit.[28] Figure 3 shows the recording of $u(\boldsymbol{x}_B, \boldsymbol{x}, t)$, the wavefield measured at $\boldsymbol{x}_B$ for each source location $\boldsymbol{x}$ as the source is translated in a circle encircling the receivers. The total wavefield can be written as the sum of the direct wave u_0 and the waves u_i that are radiated by each scatterer i. Note that u_i is dominated by the single-scattered waves, but it also contains contributions from multiple scattering interactions with other scatterers. The wavefield is then given by

$$u = u_0 + \sum_{i=1}^{N} u_i, \tag{11}$$

where N is the total number of scatterers. Recording of $u(\boldsymbol{x}_B, \boldsymbol{x}, t)$ is done by blocking the vibrometer sample beam that would detect $u(\boldsymbol{x}_A, \boldsymbol{x}, t)$, the wavefield at $\boldsymbol{x}_A$. The $\boldsymbol{x}$ coordinates are presented as a function of source azimuth ($0^\circ < \theta < 360^\circ$) with respect to the center of the aluminum block, where $\theta = 0^\circ$ corresponds to the bottommost point of the circle. Figure 3 is dominated by a direct Rayleigh wave, the first term in Eq. (11), which travels from the source to the receiver at a velocity of 2900 ms^{-1} in the aluminum block.

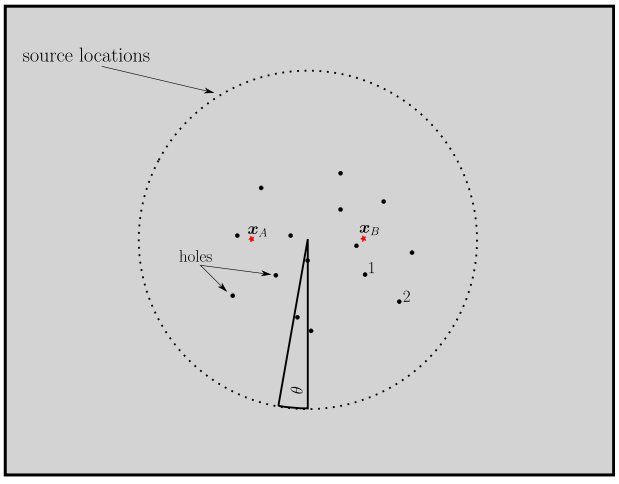

FIG. 2. (Color online) In an aluminum block with 15 holes, $\boldsymbol{x}_A$ and $\boldsymbol{x}_B$ mark the locations where the wavefield is recorded with a dual-beam interferometer. The elastic wave source is moved in a circle around the scatterers and the recording locations. The position of the source is recorded as a function of the angle θ, where $\theta = 0$ is defined by the bottom most point of the circle. Hole 1 is located 52.5 mm and 15.5 mm from $\boldsymbol{x}_A$ and $\boldsymbol{x}_B$, respectively. Hole 2 is located 72 mm and 32 mm from $\boldsymbol{x}_A$ and $\boldsymbol{x}_B$, respectively.

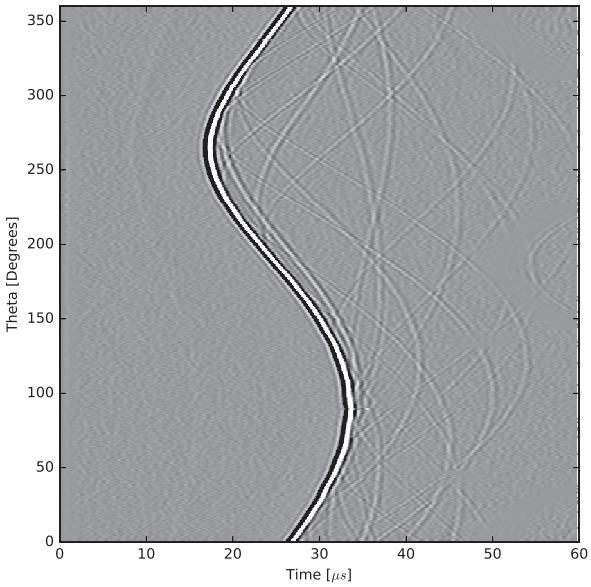

FIG. 3. Elastic wavefields recorded by the interferometer with only the $\boldsymbol{x}_B$ sample beam incident on the block, presented as a function of the excitation angle. The greyscale image shows the surface particle motion of the aluminum block where white and black shades represent motion into and out of the surface, respectively. The dominant feature is the direct Rayleigh wave arrival from source to receiver. Rayleigh waves scattered by holes in the surface of the aluminum block are detected at lower amplitudes and later arrival times.

In the greyscale image, whiter and darker shades represent particle motion away from and toward the vibrometer, respectively. As the source is translated in a circle around the center of the aluminum block the arrival time of the direct wave varies sinusoidally as $\boldsymbol{x}_B$ is positioned 2.5 cm away from the center of the circle with sources. Waves scattered by the holes in the aluminum block, represented by u_i in Eq. (11), show up in the recorded wavefield at times greater than the direct arrival and at lower amplitudes. Multiply scattered waves do not show up above the noise floor of our data and we ignore these in our analysis.

Next, we repeat our translation with both vibrometer sample beams incident on the aluminum block. Figure 4 shows the recording of $u(\boldsymbol{x}_A, \boldsymbol{x}, t) + u(\boldsymbol{x}_B, \boldsymbol{x}, t)$ for each source location. As the wavefield for each shot is the sum of two receiver locations, two large amplitude direct Rayleigh waves show up as sinusoids in Fig. 4. Smaller amplitude vibrations due to scattering of waves from holes in the surface of the aluminum block are also present in the recorded wavefield sum.

V. RESULTS: ESTIMATING THE GREEN'S FUNCTION WITH AUTOCORRELATIONS

Equation (11) describes a wavefield comprised of a direct wave and many waves radiated by scatterers. The autocorrelation of this wavefield is, in the frequency domain, given by

$$|u|^2 = |u_0|^2 + \sum_{i=1}^{N} |u_i|^2 + \sum_{i=1}^{N} (u_i u_0^* + u_i^* u_0) + \sum_{i \neq j} u_i u_j^*. \tag{12}$$

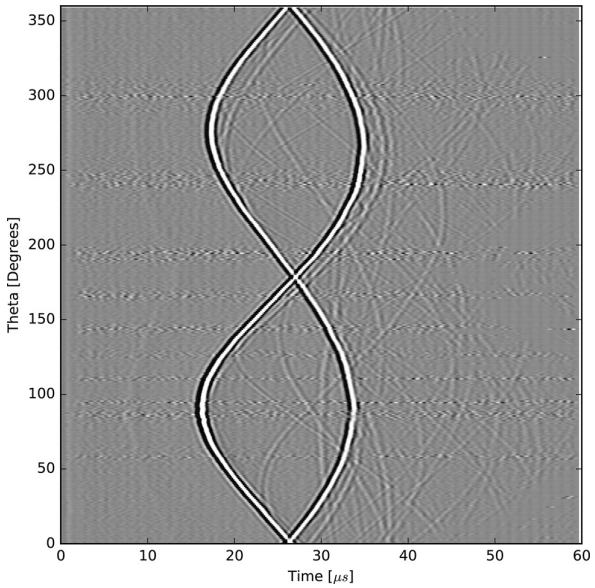

FIG. 4. Elastic wavefields at $\boldsymbol{x}_A$ and $\boldsymbol{x}_B$ recorded by the interferometer recordings are presented as a function of the excitation angle. The direct Rayleigh wave for each receiver can be identified as large amplitude sinusoids. Waves scattered by holes in the surface of the aluminum block can be observed after the direct wave arrival at lower amplitudes.

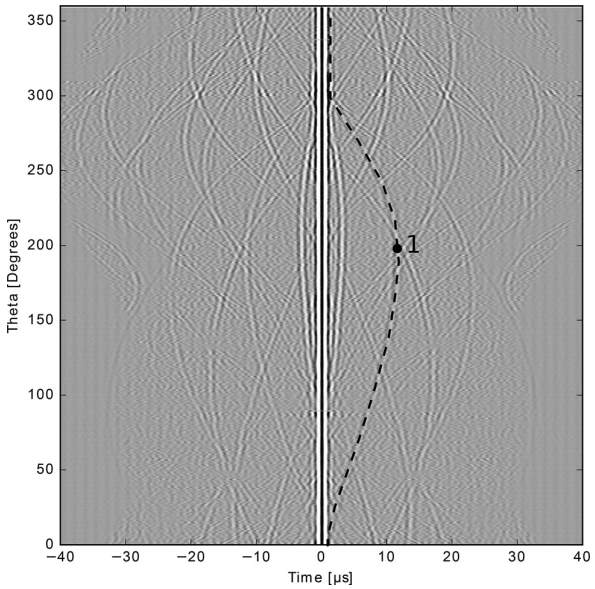

FIG. 5. Autocorrelation of the wavefield recorded at $\boldsymbol{x}_B$ for each source position, θ. The autocorrelation of the recorded wavefield is dominated by strong oscillations near $t \approx 0$, which corresponds to the "direct" Rayleigh wave from $\boldsymbol{x}_B$ to $\boldsymbol{x}_B$. Waves scattered by holes are present in the coda of the autocorrelation and vary smoothly in time as a function of θ. The dashed line follows the correlation of the direct wave and a scattered wave for each source location. This scattered wave has an maximum arrival time of $t \approx -10.7\ \mu$s at $\theta \approx 200°$, which corresponds to hole 1 in Fig. 2.

The first two terms are the autocorrelation of a wave with itself, which peaks at $t = 0$. The terms $u_i u_0^*$ is the cross-correlation of the direct wave with the wave radiated by scatterer i; this term gives an arrival at the difference of the arrival time of u_i relative to the direct waves. The term $u_i^* u_0$ is the same but at the opposite arrival times. Finally, the cross terms $u_i u_j^*$ for $i \neq j$ are of higher order in the scattered waves and are, in general, small compared to the cross terms $u_i u_0^*$ and $u_i^* u_0$. When we ignore products of scattered waves, Eq. (12) reduces to

$$|u|^2 \approx |u_0|^2 + \sum_{i=1}^{N} (u_i u_0^* + u_i^* u_0)\,. \tag{13}$$

Figure 5 shows the autocorrelation of each shot of $u(\boldsymbol{x}_B, \boldsymbol{x}, t)$ shown in Fig. 3. The sum of these autocorrelations approximates $G(\boldsymbol{x}_B, \boldsymbol{x}_B, \omega)S(\omega)$ in Eq. (4), where $G(\boldsymbol{x}_B, \boldsymbol{x}_B, \omega)$ is the Green's function for a coinciding source and receiver located at $\boldsymbol{x}_B$.[8] In this case the "direct" Rayleigh wave is instantaneous and arrives at $t = 0$. In the autocorrelation, the delay time of scattered waves is the difference in arrival time between the direct wave and scattered wave for each wavefield in Fig. 3. The delay time for scattered waves varies smoothly as a function of the source position θ. Extrema in the delay time for a given scattered wave defines the stationary phase point, indicating the position where the source, receiver, and scatterer are aligned.[8] The dashed line in Fig. 5 follows the delay time of a scattered wave, relative to the direct wave, with an extrema of $t \approx +10.7\ \mu$s. Because the autocorrelation is symmetric in time, as shown in Eq. (12), there is an identical stationary-phase point at $t \approx -10.7\ \mu$s. Using the aluminum Rayleigh wave speed, the distance between x_B and the scatterer is calculated to be $r = 15.5$ mm, which corresponds to hole 1 in Fig. 2. For two receivers recorded in a single channel, Eq. (4) indicates the autocorrelation of the sum of a wavefield recorded at two locations can be used to approximate the Green's function between the two locations, $G(\boldsymbol{x}_A, \boldsymbol{x}_B, \omega)S(\omega)$. Figure 6 displays the autocorrelation of each wavefield presented in Fig. 4. The autocorrelation function is dominated by large amplitudes near $t = 0$, corresponding to the $G(\boldsymbol{x}_A, \boldsymbol{x}_A, \omega)S(\omega)$ and $G(\boldsymbol{x}_B, \boldsymbol{x}_B, \omega)S(\omega)$ terms in Eq. (4). The direct wave between receivers shows up as sinusoids in the autocorrelation also, corresponding to the $G(\boldsymbol{x}_A, \boldsymbol{x}_B, \omega)S(\omega)$ term in Eq. (4). To extract the Green's function, we sum the wavefields in Fig. 6 over the source position. The time-reversed anti-causal recording ($t < 0$) is then summed with the causal recording to improve the SNR. Figure 7 shows the extracted Green's function using the autocorrelation method, compared to the Green's function extracted by standard seismic interferometry from individual recordings of wavefields $u(\boldsymbol{x}_A, \boldsymbol{x}, t)$ and $u(\boldsymbol{x}_B, \boldsymbol{x}, t)$. The arrows indicate where scattered waves are expected to arrive based on the distances from each scatterer to the receivers.

VI. DISCUSSION

We used transient sources to generate an equipartitioned wavefield of which the autocorrelation function can be applied to extract the Green's function. Equation (4) shows that the autocorrelation is comprised of the Green's function between receivers and the Green's function for coinciding source and receivers located at $\boldsymbol{x}_A$ and $\boldsymbol{x}_B$. The coinciding source and receiver terms cause artefacts to occur throughout

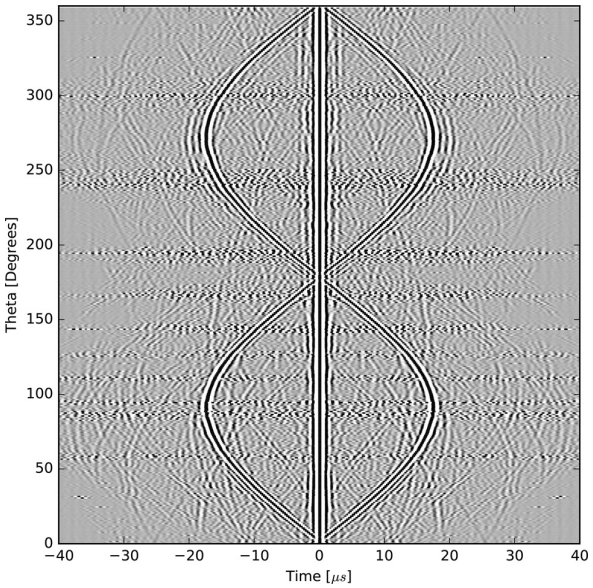

FIG. 6. Autocorrelation of the dual wavefield as a function of the source angle θ. As in Fig. 5, the autocorrelation is dominated by strong oscillations near $t \approx 0$, which correspond to the direct Rayleigh wave from $\boldsymbol{x}_A$ to $\boldsymbol{x}_A$ and from $\boldsymbol{x}_B$ to $\boldsymbol{x}_B$. The direct wave that travels between $\boldsymbol{x}_A$ and $\boldsymbol{x}_B$ shows up as large amplitude sinusoids that oscillate about $t = 0$ with extrema of $t \approx 17\,\mu$s.

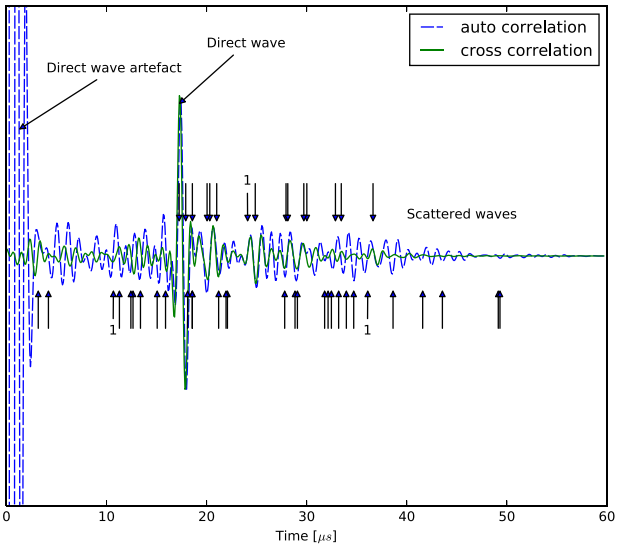

FIG. 7. (Color online) The sum of the autocorrelated wavefields (dashed) is compared to the Green's function extracted using standard seismic interferometry (solid). The direct wave has an arrival time of $t \approx 17\,\mu$s and a good agreement is found between the autocorrelation and the Green's function. The autocorrelation is dominated by a direct wave artefact, which occurs at $t = 0\,\mu$s. Arrows show when waves scattered by the holes are expected to arrive and are calculated using the co-ordinates of the holes and $\boldsymbol{x}_A$ and $\boldsymbol{x}_B$. Upper arrows indicate the arrival times of waves that are emitted from one receiver, scattered by holes in the aluminum, and then detected by the opposing receiver. These waves are present in both the cross-correlation and the autocorrelation. Lower arrows indicate the arrival times of waves that are emitted and detected by the same receiver after being backscattered from the holes. Arrows labeled 1 show where waves scattered by hole 1 are expected to occur in the cross- and autocorrelations.

the autocorrelation. Near $t = 0$ artefacts are due to the direct Rayleigh wave at both $\boldsymbol{x}_A$ and $\boldsymbol{x}_B$, and later artefacts are caused by waves that have been backscattered by holes to and from the same location. Because of these terms, we expect a single hole to produce three scattered waves in the autocorrelation, one for each component of Eq. (4): $G(\boldsymbol{x}_A, \boldsymbol{x}_B, \omega)S(\omega)$, $G(\boldsymbol{x}_A, \boldsymbol{x}_A, \omega)S(\omega)$ and $G(\boldsymbol{x}_B, \boldsymbol{x}_B, \omega)S(\omega)$. In Fig. 7, the upper arrows indicate the expected scattered wave arrival times for the $2\Re[G(\boldsymbol{x}_A, \boldsymbol{x}_B, \omega)]S(\omega)$ component, and the lower arrows indicate where artefacts occur due to $G(\boldsymbol{x}_A, \boldsymbol{x}_A, \omega)S(\omega)$ and $G(\boldsymbol{x}_B, \boldsymbol{x}_B, \omega)S(\omega)$. For example, three peaks in the autocorrelation are labeled 1, which correspond to waves scattered by the hole 1 in Fig. 2. The first of these peaks occurs at $t \approx 10.7\,\mu$s and is due to the wave that travels from $\boldsymbol{x}_B$ to 1 and is backscattered to $\boldsymbol{x}_B$. This wave arrives before the direct wave because two-way travel distance to the hole is shorter than the distance of 50 mm between $\boldsymbol{x}_A$ and $\boldsymbol{x}_B$. The next peak occurs at $t \approx 23.4\,\mu$s, corresponding to a wave that has been emitted at either $\boldsymbol{x}_A$ or $\boldsymbol{x}_B$, scattered off the hole, and then detected at the opposing receiver. The scattered wave is also present in the cross-correlation. The third peak occurs at $t \approx 36\,\mu$s, corresponding to the wave that makes a round trip from $\boldsymbol{x}_A$ to the hole. This scattered wave coincides with the wave that is scattered by hole 2 in the cross-correlation. For the direct wave between receivers, which has an arrival time of $t \approx 17\,\mu$s, there is a good agreement between the autocorrelation of the wavefield sum and the cross-correlation of the individual wavefields. At times before the direct wave arrival, the autocorrelation has artefacts corresponding to events that are backscattered from a coinciding source and receiver and the instantaneous direct wave arrival, as shown in Figs. 5 and 6. From $17 < t < 27\,\mu$s few artefacts occur and again there is good agreement between the Green's function and autocorrelation. For $t < 27\,\mu$s, many artefacts occur in the autocorrelation and agreement with the Green's function is diminished. Without prior knowledge of the location of scatterers it is not possible to differentiate between artefacts and scattered waves in the Green's function, other than those that occur before the direct wave arrival between receivers. The terms $G(\boldsymbol{x}_A, \boldsymbol{x}_A, \omega)S(\omega)$ and $G(\boldsymbol{x}_B, \boldsymbol{x}_B, \omega)S(\omega)$ in Eq. (4), which are the cause of artefacts in the autocorrelation of the wavefield sum, can be subtracted from the resultant Green's function to remove the artefacts if they have been recorded separately. In practice, to completely remove the artefacts both $u(\boldsymbol{x}_A, \boldsymbol{x}, t)$ and $u(\boldsymbol{x}_B, \boldsymbol{x}, t)$ would need to be recorded and their autocorrelations subtracted from the wavefield sum autocorrelation. Furthermore, with $u(\boldsymbol{x}_A, \boldsymbol{x}, t)$ and $u(\boldsymbol{x}_B, \boldsymbol{x}, t)$ recorded individually $G(\boldsymbol{x}_A, \boldsymbol{x}_B, \omega)S(\omega)$ can be estimated via the cross-correlation of these wavefields, making the autocorrelation of the wavefield sum redundant. For *in situ* structural health monitoring, we propose not to use active sources but long recordings of the ambient background elastic wavefield. In this case, artefacts that are present in the autocorrelation of the wavefield recorded at two locations may not be detrimental to monitoring changes in a material. Artefacts occur because of scatterers in the material, therefore, the arrival time of artefacts are indicative of changes in the Green's function between receivers and could be used for monitoring. Changes in Green's function could be estimated by monitoring changes in the autocorrelation over time, similar

to standard monitoring techniques.[6] The cost of laser Doppler vibrometers plays a major role in the prevalence of contacting transducers for non-destructive testing. This becomes an even greater problem when two locations are required to be sampled simultaneously. Our LDV design does not require a large number of additional components, reducing the costs. Furthermore, because the interferometer records the sum of two wavefields in a single channel, the number of acquisition channels and data size do not increase compared to a traditional laser Doppler vibrometer.

VII. CONCLUSION

We present underlying theory and hardware required to estimate the Green's function between two locations using the autocorrelation of the sum of equipartitioned wavefields. This technique is an adaption from standard seismic interferometry where the correlation function is applied to independent receivers. Furthermore, a dual-beam laser interferometer capable of recording the sum of a wavefield measured at two locations is presented in detail. Such a device and technique could provide a low-cost, non-contact method of characterizing *in situ* material properties. As a proof of concept, we approximate the direct Rayleigh-wave Green's function and scattered coda between two locations on an aluminum block with surface scatterers using the autocorrelation. The Green's function is compared to that estimated by traditional seismic interferometry, highlighting large artefacts that occur near $t = 0$. Our technique requires few modifications to traditional seismic and laser interferometry and could be applied to passive structural monitoring.

[1]K. Aki, "Space and time spectra of stationary stochastic waves, with special reference to microtremors," Bull. Earth. Res. Inst. **35**, 415–456 (1957).
[2]M. Campillo and A. Paul, "Long-range correlations in the diffuse seismic coda," Science **299**(5606), 547–549 (2003).
[3]R. Snieder and E. Şafak, "Extracting the building response using seismic interferometry: Theory and application to the Millikan Library in Pasadena, California," Bull. Seismol. Soc. Am. **96**(2), 586–598 (2006).
[4]A. Curtis, P. Gerstoft, H. Sato, R. Snieder, and K. Wapenaar, "Seismic interferometry: Turning noise into signal," The Leading Edge **25**(9), 1082–1092 (2006).
[5]O. I. Lobkis and R. L. Weaver, "On the emergence of the Green's function in the correlations of a diffuse field," J. Acoust. Soc. Am. **110**(6), 3011–3017 (2001).
[6]C. Sens-Schönfelder and U. Wegler, "Passive image interferometry and seasonal variations of seismic velocities at Merapi Volcano, Indonesia," Geophys. Res. Lett. **33**(21), L21302, https://doi.org/10.1029/2006GL027797 (2006).
[7]A. E. Malcolm, J. A. Scales, and B. A. van Tiggelen, "Extracting the Green's function from diffuse, equipartitioned waves," Phys. Rev. E **70**(1), 015601 (2004).
[8]T. D. Mikesell, K. van Wijk, T. E. Blum, R. Snieder, and H. Sato, "Analyzing the coda from correlating scattered surface waves," J. Acoust. Soc. Am. **131**(3), EL275–EL281 (2012).
[9]K. G. Sabra, P. Roux, and W. Kuperman, "Emergence rate of the time-domain Green's function from the ambient noise cross-correlation function," J. Acoust. Soc. Am. **118**(6), 3524–3531 (2005).
[10]K. Wapenaar and J. Fokkema, "Green's function representations for seismic interferometry," Geophysics **71**(4), SI33–SI46 (2006).
[11]A. Grêt, R. Snieder, and U. Özbay, "Monitoring *in situ* stress changes in a mining environment with coda wave interferometry," Geophys. J. Int. **167**(2), 504–508 (2006).
[12]R. Snieder and M. Hagerty, "Monitoring change in volcanic interiors using coda wave interferometry: Application to Arenal volcano, Costa Rica," Geophys. Res. Lett. **31**(9), L09608, https://doi.org/10.1029/2004GL019670 (2004).
[13]R. Snieder, A. Grêt, H. Douma, and J. Scales, "Coda wave interferometry for estimating nonlinear behavior in seismic velocity," Science **295**(5563), 2253–2255 (2002).
[14]C. R. Farrar and G. H. James III, "System identification from ambient vibration measurements on a bridge," J. Sound Vib. **205**(1), 1–18 (1997).
[15]S. C. Stähler, C. Sens-Schönfelder, and E. Niederleithinger, "Monitoring stress changes in a concrete bridge with coda wave interferometry," J. Acoust. Soc. Am. **129**(4), 1945–1952 (2011).
[16]U. Wegler, B.-G. Lühr, R. Snieder, and A. Ratdomopurbo, "Increase of shear wave velocity before the 1998 eruption of Merapi Volcano (Indonesia)," Geophys. Res. Lett. **33**(9), L09303, https://doi.org/10.1029/2006GL025928 (2006).
[17]R. Weaver and O. Lobkis, "On the emergence of the Green's function in the correlations of a diffuse field: Pulse-echo using thermal phonons," Ultrasonics **40**(1), 435–439 (2002).
[18]S. Hitchman, K. van Wijk, N. Broderick, and L. Adam, "Heterodyne interferometry for the detection of elastic waves: A tutorial and open-hardware project," Eur. J. Phys. **36**(3), 035011 (2015).
[19]C. B. Scruby and L. E. Drain., *Laser Ultrasonics: Techniques and Applications* (Taylor and Francis, New York, 1990).
[20]S. Hitchman, K. van Wijk, and Z. Davidson, "Monitoring attenuation and the elastic properties of an apple with laser ultrasound," Postharvest Biol. Technol. **121**, 71–77 (2016).
[21]N. Muramatsu, N. Sakurai, N. Wada, R. Yamamoto, K. Tanaka, T. Asakura, Y. Ishikawa-Takano, and D. J. Nevins, "Remote sensing of fruit textural changes with a laser Doppler vibrometer," J. Am. Soc. Hortic. Sci. **125**(1), 120–127 (2000).
[22]T. E. Blum, L. Adam, and K. van Wijk, "Noncontacting benchtop measurements of the elastic properties of shales," Geophysics **78**(3), C25–C31 (2013).
[23]Y. Fujino, K. Kaito, and M. Abe, "Detection of structural damage by ambient vibration measurement using laser Doppler vibrometer," in *6th Annual International Symposium on NDE for Health Monitoring and Diagnostics*, International Society for Optics and Photonics (2001), pp. 167–178.
[24]D. Siringoringo, Y. Fujino, T. Nagayama, and H. Wenzel, "Vibration characteristics of an overpass bridge during full-scale destructive testing," Procedia Eng. **14**, 777–784 (2011).
[25]J. L. Johnson, K. van Wijk, and M. Sabick, "Characterizing phantom arteries with multi-channel laser ultrasonics and photo-acoustics," Ultrasound Med. Biol. **40**(3), 513–520 (2014).
[26]M. Morant, J. Pérez, and R. Llorente, "Polarization division multiplexing of ofdm radio-over-fiber signals in passive optical networks," Adv. Opt. Technol. **2014**, 269524 (2014)
[27]S. Haykin, *Communication Systems* (Wiley, Hoboken, NJ, 2009).
[28]J. L. Johnson, H. tom Wörden, and K. van Wijk, "PLACE an open-source python package for laboratory automation, control, and experimentation," J. Lab. Autom. **20**(1), 10–16 (2015).